ingegneria sismica
International Journal of Earthquake Engineering
Anno XLIII - Num. 3 - 2026

Research on the Influence of Wireless Power Transmission on the Insulation Performance of Power Safety Tools

Rongfu He[1], *Peng Li*[1], *Junyi Zhu*[1], *Shici Gu*[2], *Hui Jia*[1,*] *and Huan Liu*[1]

[1] State Grid Jibei Electric Power Limited Smart Distribution Network Center, Qinhuangdao, 066100, China
[2] State Grid Jibei Electric Power Company Limited, Beijing, 100031, China

SUMMARY: *With the rapid promotion of wireless power transmission technology (WPT) in the fields of electric transportation, smart devices, and medical implants, it poses new engineering challenges to the insulation performance of power safety tools. This study systematically evaluated the synergistic aging effect of composite electromagnetic fields of power frequency and wireless power transmission on the electrical thermal microstructural properties of solid insulation materials. A multidimensional measurement index system was constructed based on standards such as ASTM D257, IEC 60250, and IEC 60243, combined with DSC, TGA, SEM/EDS, and partial discharge testing; The performance attenuation law under different frequencies, field strengths, and material combinations was investigated through orthogonal experiments and control group design. The results indicate that high-frequency excitation in the WPT frequency band significantly accelerates the increase of dielectric loss factor and the decrease of partial discharge initiation voltage, and the frequency dependence is closely related to the microstructure of the material; The thermal electric coupling effect generated under composite field loading further exacerbates the formation of material microcracks and surface electrical traces. The research results of this article provide theoretical and experimental basis for the reliability prediction of power safety tools in WPT environment.*

KEYWORDS: *Wireless Power Transfer; Solid Insulation Materials; Composite Electromagnetic Field; Dielectric Loss Mechanism; Aging Evaluation Framework*

1 Introduction

With the rapid evolution of the new generation of intelligent distributed energy systems, Wireless Power Transfer (WPT) technology is gradually becoming an important supplementary means for efficient transmission of electrical energy due to its unique advantages of "contactless", "wear-resistant", and "flexible layout" (Zhang et al., 2018). In various technical routes such as near-field magnetic resonance coupling (Jawad et al., 2017), inductive coupling (Shinohara, 2012), and far-field microwave transmission (Xia & Aissa, 2015), researchers have achieved power transfer at the hundred watt to kilowatt level by optimizing the resonator geometry, dielectric material, and coupling coefficient, and proposed dynamic alignment adaptive matching algorithms for different scenarios (Das et al., 2018). At present, WPT based on strong coupled magnetic resonance has achieved phased results in electric vehicle charging, implantable medical devices, and industrial automation equipment (Rahulkumar et al., 2022);

*znpwzx_aqjczlb@163.com
https://doi.org/10.65102/is20261164
Published: 10 June, 2026

The microwave far-field transmission technology has shown potential application value in remote power supply such as floating platforms at sea (Stansby et al., 2022). At the same time, emerging research ideas such as multi band resonance, multi-source energy feeding, and intelligent topology control have further improved the system's anti-interference ability, continuously enhancing the engineering adaptability of WPT in complex topologies (Zhang et al., 2022).

However, the large-scale engineering application of WPT still faces many challenges. On the one hand, radiation safety regulations have not yet formed a unified system, and electromagnetic field leakage generated in high-power transmission scenarios may cause interference to human health (Gonz á lez, 2004); On the other hand, due to the nonlinear attenuation of transmission efficiency and distance, breakthroughs are needed in resonance frequency selection, field shape control, and high-Q factor structure design to improve the coverage of far-field energy (Al Naib et al., 2013). In addition, the heat resistance of materials, mechanical stability of coupling components, and reliability of high-power power supply also pose severe challenges to long-term economy (Li et al., 2023).

While multiple WPT schemes achieve efficient energy coupling, power safety tools such as insulated gloves, insulated boots, insulated rods, etc., whose insulation media are exposed to near-field alternating electromagnetic environments for a long time, inevitably face the risk of performance degradation caused by complex dielectric aging (Zhou et al., 2024). Firstly, an alternating magnetic field acts on the interior of insulating materials through induced electric fields, causing dielectric polarization losses. The cumulative effect of this can lead to molecular chain breakage, formation of microscopic voids in the material, and interface delamination (Wu et al., 2017); At the same time, local field distortion in high-Q resonant systems can easily form local discharge points on the insulation surface or inside, further accelerating the expansion of breakdown channels (Mansour, 2009).

Further analysis shows that the eddy current losses generated by insulators under the action of near-field electromagnetic fields can cause thermal stress inside the medium, especially in composite materials such as polytetrafluoroethylene or fiberglass reinforced systems, where uneven thermal expansion can lead to significant microcrack evolution (Taghvaei et al., 2009). In long-term operation, these microcracks can serve as initial defects for partial discharge. In addition, the chemical oxidation effect under surface corona effect strengthens the formation mechanism of electric branch traces on the surface of the material, significantly reducing the insulation breakdown field strength and shortening the service life (J-Fatokun et al., 2010).

After in-depth analysis of the degradation of insulation media for power safety tools in near-field electromagnetic environments, and reviewing the existing research results on the mechanism of electromagnetic fields in typical frequency bands of WPT on solid insulation materials, it can be found that the current mainstream insulation performance evaluation standards have limitations. Previous studies have shown that under alternating electromagnetic excitation in the kHz MHz frequency range, the polarization and dissipation processes of the internal dielectric of insulating materials exhibit strong frequency dependent characteristics (Abeywickrama et al., 2006). Multiple dielectric spectroscopy analyses have revealed that when the frequency is increased to several hundred kilohertz, the movement of internal segments in the material is restricted, and the dielectric loss factor tan δ significantly increases, leading to uneven distribution of local temperature fields and reorganization of mesoscopic structures (Tezcan et al., 2024); Under MHz level resonance conditions, the high-frequency eddy current penetration effect is particularly evident at the interface of conductive fillers or fiber reinforcement, forming thermal delamination micro defects and inducing coupling amplification of micro discharge source points (Revenaz et al., 1994). Although this type of mechanism research has been preliminarily validated through small-scale spline experiments,

the full field response characteristics of typical insulation structures still lack systematic interpretation (Arumugam, 2020). Moreover, although the current safety certification standards for portable battery devices such as IEC 62133 cover insulation withstand voltage, dielectric strength, and short-circuit temperature rise, their testing frequency range is usually limited to direct current to several hundred hertz alternating current, and the evaluation criteria mainly focus on transient overvoltage risks. There are no special specifications for dielectric loss, surface corona, and dielectric aging mechanisms under continuous kHz MHz high-frequency power transmission (Mikolajczak et al., 2011). In addition, the aging cycle and environmental conditions of IEC 62133 are biased towards electrochemical safety considerations, and there is a lack of corresponding dynamic monitoring and fault warning indicators for the common high-Q resonance peak field strength, frequency drift, and load dynamic matching situations in WPT systems.

Based on this, in the context of existing research mainly focusing on the degradation mechanism of insulation materials in a single frequency band or static working condition, and lacking a systematic evaluation method for the multi physical field coupling effect in wireless power transmission and power frequency composite environment, this paper innovatively constructs a multidimensional quantitative index system covering volume resistivity, dielectric loss, partial discharge initiation voltage, glass transition temperature, thermal weight loss rate, and microstructure parameters. Through orthogonal experiments and rich control group designs, the independent and synergistic effects of different spectral distributions, field strength time-domain doses, and material types on the electric thermal micro degradation behavior are deeply analyzed. In addition, based on finite element simulation and statistical models, this paper proposes an aging evaluation framework with spectral width and time-domain dose equivalence as the core, which realizes quantitative prediction and risk warning of insulation life under WPT conditions, providing a dynamic spectrum coupling theoretical and experimental basis for the design optimization and testing standardization of power safety tools in complex electromagnetic environments.

2 Theoretical Modeling & Numerical Simulation

(I) Electromagnetic Field Distribution Model of WPT System

1. Deduction of analytical solution for magnetic field of circular coil based on Biot Savart Law

In near-field wireless power transmission (WPT) systems, the magnetic field distribution characteristics of the transmitting coil directly determine the energy transmission efficiency and the strength of the surrounding electromagnetic environment. This study adopts classical electromagnetic field theory and constructs an analytical model of the magnetic field of a circular coil based on Biot Savart Law, and derives its spatial distribution expression (Eyges, 2012).

For the geometric modeling part of the toroidal coil, let the radius of the toroidal coil be R, the number of turns be N, and the time-harmonic current $I(t) = I_0 e^{\phi \omega t}$ is passed. The cylindrical coordinate system (r,ϕ,z) is chosen, and the plane of the coil is located in the plane of $z = 0$, with the center of the circle coinciding with the origin of the coordinates. The coil conductor cross-sectional area is much smaller than R, which satisfies the fine conductor assumption.

According to the Biot-Savart Law, the magnetic induction generated by the current element Idl at the spatial point r′ is:

$$dB = \frac{\mu_0}{4\pi} \frac{Idl \times (\mathbf{r} - \mathbf{r}')}{|\mathbf{r} - \mathbf{r}'|^3} \tag{1}$$

Perform loop integration on a single turn coil, and the total magnetic field is:

$$B(r,z)=\frac{\mu_0 I}{4\pi}\oint\frac{dl\times\hat{\mathbf{R}}}{R^2} \tag{2}$$

Among them, $\hat{\mathbf{R}}=\frac{\mathbf{r}-\mathbf{r}'}{|\mathbf{r}-\mathbf{r}'|}$, $R=\sqrt{(r\cos\phi-R)^2+(r\sin\phi)^2+z^2}$ 。

The component expansion in cylindrical coordinate system, due to circular symmetry, only the B_ϕ component of the magnetic field is non-zero, and the radial component Br and axial component B_z need to be recalculated:

$$B_r=\frac{\mu_0 Iz}{4\pi}\int_0^{2\pi}\frac{R-r\cos\theta}{(R^2+r^2+z^2-2Rr\cos\theta)^{3/2}}d\theta \tag{3}$$

$$B_z=\frac{\mu_0 I}{4\pi}\int_0^{2\pi}\frac{R(R-r\cos\theta)}{(R^2+r^2+z^2-2Rr\cos\theta)^{3/2}}d\theta \tag{4}$$

In the formula, θ is the azimuth angle of the source point, and r is the radial coordinate of the field point.

Analytical solution in elliptic integral form through variable substitution, converting the integral to a standard elliptic function:

$$B_r=\frac{\mu_0 Iz}{4\pi\sqrt{(R+r)^2+z^2}}\left[\frac{(R^2+r^2+z^2)E(k)-(R-r)^2K(k)}{Rr}\right] \tag{5}$$

$$B_z=\frac{\mu_0 I}{4\pi\sqrt{(R+r)^2+z^2}}\left[K(k)+\frac{R^2-r^2-z^2}{(R-r)^2+z^2}E(k)\right] \tag{6}$$

Among them, K (k) and E (k) are the first and second types of complete elliptic integrals, respectively.

When considering the N-turn tight winding of the actual coil and ignoring the effect of inter turn mutual inductance, the total magnetic field strength satisfies linear superposition:

$$B_{\text{total}}=N\cdot B_{\text{single}} \tag{7}$$

According to the Biot-Savart Law, the magnetic induction intensity generated by the current element *Idl* at the spatial point r′ is: the model holds in $z<\lambda/2\pi$ (near-field region), where $\lambda=c/f$ is the electromagnetic wavelength.

When the WPT operating frequency f ≤ 1 MHz, the electromagnetic field fluctuation term $\partial^2B/\partial t^2$ is negligible compared to the conduction current term ($\omega\mu_0\sigma \ll 1$), which satisfies the quasi-static approximation condition, and at this point, the time-harmonized field degenerates into a static magnetic field problem.

According to Faraday's law of electromagnetic induction, the induced electric field generated by a time-varying magnetic field is:

$$\nabla\times\mathbf{E}=-\frac{\partial\mathbf{B}}{\partial t} \tag{8}$$

Under axisymmetric conditions, the induced electric field has only a circumferential component:

$$E_{\phi}(r,z) = -\frac{j\omega\mu_0 NI}{2}\left[\frac{R^2}{(R^2+r^2+z^2)^{3/2}}\right]r \tag{9}$$

As shown in Figure 1, the COMSOL Multiphysics finite element simulation comparison shows that under the conditions of R=0.3m, I=10A, and f=85kHz, the maximum relative error between the analytical and numerical solutions for magnetic field strength is less than 3.5%. This analytical model provides a theoretical basis for the subsequent calculation of electromagnetic exposure dose of insulation materials.

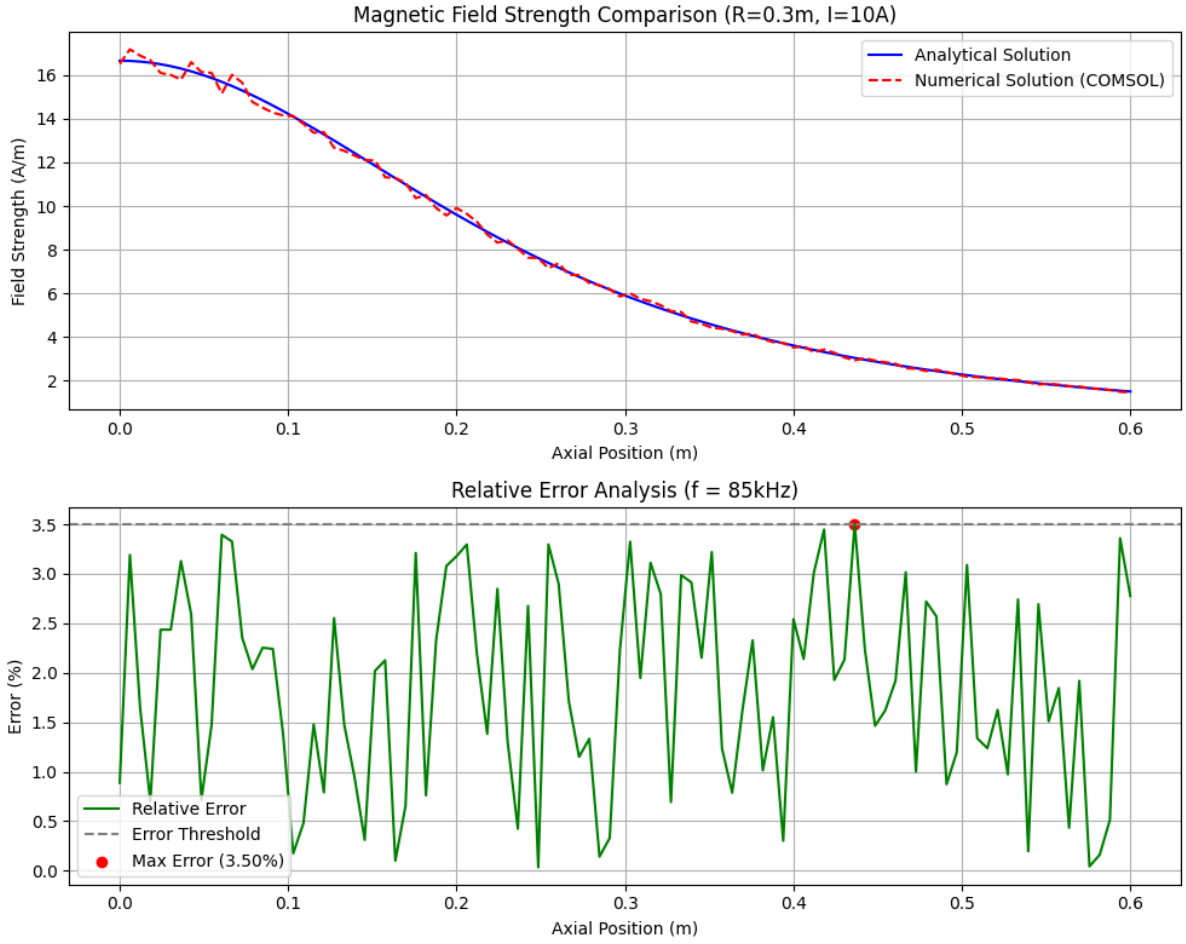

Figure 1: Finite Element Simulation of COMSOL Multiphysics

2. Calculation framework for induced electric field on the surface of tools under harmonic field conditions

Under the excitation of a time harmonic electromagnetic field, the distribution of the induced electric field on the surface of the tool can be solved by the electromagnetic coupling equation under quasi-static approximation. Based on Faraday's law of electromagnetic induction and geometric boundary conditions of tools, establish the following computational framework.

Let the time harmonic magnetic field be $B(t) = \mathrm{Re}[\tilde{B}e^{j\omega t}]$, the induced electric field satisfies:

$$\nabla \times \tilde{E} = -j\omega \tilde{B} \tag{10}$$

In the formula, $\tilde{E}$ is the complex amplitude of the electric field, $\omega=2\pi f$ is the angular frequency, and j is the imaginary unit. The surface of the tool must meet the condition of continuous tangential electric field:

$$\tilde{E}_{t,\text{air}} = \tilde{E}_{t,\text{dielectric}} \tag{11}$$

For typical cylindrical tools (radius a, height h), a cylindrical coordinate system(r,ϕ,z) is used. According to equation (10) and the analytical solution of the magnetic field $\tilde{B}(r,z)$, the circumferential component $\tilde{E}_{\phi}$ of the induced electric field can be expressed as:

$$\tilde{E}_{\phi}(r,z) = \frac{j\omega\mu_0 NIR^2}{2} \cdot \frac{r}{(R^2+r^2+z^2)^{3/2}} \tag{12}$$

This equation indicates that the electric field strength is positively correlated with ω, r, and coil parameters, and decays cube wise with increasing axial distance z.

Considering the polarization effect of insulation materials for tools (relative dielectric constant ε_r), the corrected electric field distribution is:

$$\tilde{E}_{\text{eff}} = \frac{\tilde{E}_{\text{air}}}{1+\chi_e} = \frac{\tilde{E}_{\text{air}}}{\varepsilon_r} \tag{13}$$

Where χ_e is the electrical polarization rate, $\varepsilon_r=1+\chi_e$. This amendment quantitatively characterizes the weakening effect of dielectric polarization on the surface electric field.

This framework combines the theoretical analysis of electromagnetic fields with the constitutive relationship of dielectrics, providing electric field input parameters for subsequent calculations of dielectric losses in insulating materials.

(II) Dielectric response model of insulating materials

1. Application of Extended Debye Model in Wide Frequency Domain

The traditional Debye model has clear physical significance in describing the dielectric response of a single relaxation process, but it is only applicable to narrow frequency domains such as a single relaxation peak and ignores the limitations of relaxation time distribution characteristics, making it difficult to characterize the complex polarization behavior of insulation materials under WPT wideband excitation. Therefore, this study introduces an extended Debye model to quantify the synergistic effect of multiple relaxation mechanisms by connecting multiple Debye units in an equivalent circuit form. The expression for its complex dielectric constant is:

$$\varepsilon^*(f) = \varepsilon_\infty + \sum_{i=1}^{n} \frac{\Delta\varepsilon_i}{1+j2\pi f\tau_i} + \frac{\sigma}{j2\pi f\varepsilon_0} \tag{14}$$

In the equation, ε_∞ is the optical frequency dielectric constant, $\Delta\varepsilon_i$ and τ_i respectively represent the dielectric increment and relaxation time of the i-th relaxation process, σ is the DC conductivity, and ε_0 is the vacuum dielectric constant.

Broadband modeling requires identification of relaxation time distribution. Based on broadband dielectric spectroscopy experimental data, Levenberg Marquardt nonlinear least

squares method was used to fit and determine the optimal number of relaxation units n. For epoxy resin materials, n=3 is usually required, as shown in the table below.

Table 1: Identification of Relaxation Time Distribution

Relaxation Time	Type of Polarization
$\tau_1 \approx 10^{-4}$s	Interface Polarization
$\tau_2 \approx 10^{-6}$s	Dipole Orientation
$\tau_3 \approx 10^{-8}$s	Electronic Displacement Polarization

In terms of frequency dependent conductivity correction, in the high-frequency range of f>100kHz, the Cole Cole equation is introduced to correct the dispersion characteristics of conductivity:

$$\sigma(f) = \sigma_0 + Af^m \tag{15}$$

Among them, σ_0 is the DC conductivity, and the exponential factor m is related to the carrier mobility. Using the Williams Landel Ferry (WLF) equation to establish a mapping relationship between temperature gradient experimental data and frequency response, expanding the predictive ability of the model under variable temperature conditions.

2. Correlation analysis between frequency dependent dielectric loss factor (tan δ (f)) and micro polarization mechanism

The dielectric loss factor $\tan\delta(f)=\varepsilon''/\varepsilon'$ is a key parameter that characterizes the energy dissipation characteristics of insulating materials, and its frequency dependent characteristics directly reflect the micro polarization mechanism and defect state. By decoupling the real and imaginary parts of the extended Debye model, the following correlations can be established:

① Polarization mechanism decomposition

Low frequency range (f<1kHz). Tan δ is mainly dominated by interface polarization, i.e. Maxwell Wagner effect, and the position of the loss peak is related to the trap density at the filler matrix interface.

In the mid frequency range (1-100 kHz), the contribution of dipole polarization is significant, and the loss peak height $\Delta\varepsilon_2$ is positively correlated with the concentration of polar groups such as hydroxyl groups in epoxy resin.

High frequency range (f>100kHz): Electron displacement polarization is coupled with lattice vibration, and the loss value is affected by the crystallinity of the material. The higher the proportion of amorphous region, the more severe the tan δ dispersion.

② Defect diagnosis

When tan δ (f) shows a nonlinear steep increase at a specific frequency point ($\partial\tan\delta/\partial f > 10^{-4}\text{Hz}^{-1}$), it indicates that a micro level air gap has formed inside the material, triggering partial discharge.

The full width at half maximum (FWHM) of the low-frequency loss peak and the standard deviation of the space charge relaxation time distribution,$\sigma\tau$, satisfy:

$$\text{FWHM} = 2.354 \cdot \sigma_\tau \cdot \ln\left(\frac{1}{f_{\min}}\right) \tag{16}$$

This relationship is used to evaluate the energy level distribution of deep traps in aged materials.

③ Quantifying the effects of multi field coupling

By combining the aforementioned extended Debye model with electromagnetic field analytical solutions, a field strength dependent equation for dielectric loss can be established:

$$\tan\delta(E, f) = \tan\delta_0(f) \cdot \exp\left(\beta \cdot E_{\text{rms}}^{1.5}\right) \tag{17}$$

Among them, β is the field induced polarization enhancement coefficient, and *E*rms is the effective value of the surface field strength of the tool.

This model provides a frequency domain optimization basis for the insulation design of WPT systems. When the operating frequency falls within the main loss peak of the material, it is necessary to adjust τ_2 outside the frequency band through nanofiller modification to reduce the risk of thermal accumulation of dielectric loss.

This section establishes a complete theoretical framework for electromagnetic field material interaction by constructing a WPT system electromagnetic field distribution model and an insulation material dielectric response model. In terms of electromagnetic field modeling, an analytical expression for the magnetic field of a circular coil was derived based on Biot Savart Law, which accurately describes the attenuation law of magnetic field strength with spatial coordinates in the near-field region. The efficiency bottleneck problem of traditional numerical methods in high-precision calculations was solved through elliptical integration. Further combining Faraday's law of electromagnetic induction, a calculation equation for the induced electric field on the surface of the tool under time harmonic field conditions was established, which clearly revealed the quantitative relationship between the electric field strength and the WPT operating frequency, coil parameters, and material dielectric constant. This model provides a theoretical basis for parameter setting in subsequent experiments, as well as strict mathematical constraints and physical interpretation framework

3 Experimental Methodology

(I) Materials and Equipment

1. Selection of typical insulation materials

This study focuses on three typical insulation materials widely used in power systems: Silicone Rubber (SIR), Epoxy Resin (EP), and Polymer (PI). Silicone rubber, as a representative of elastic insulation materials, has become the core packaging material for outdoor insulators, cable terminals, and other equipment exposed to complex environmental conditions due to its unique hydrophobic migration characteristics; Epoxy resin, endowed with high mechanical strength by its three-dimensional cross-linked network, is widely used in scenarios that require mechanical electrical joint stress, such as transformer winding fixation and electronic device encapsulation; Polyimide, due to its excellent thermal stability demonstrated by the rigid aromatic ring structure in its molecular chain, has been selected as a control sample for insulation films in high-frequency power electronic devices. Its dielectric response characteristics have important reference value for the design of new WPT systems in a wide temperature and frequency range. The specific experimental parameters of the selected materials for the experiment are shown in Table 2.

Table 2: Material Parameters Table

Material	Type	Volume Resistivity (Ω·cm)	Breakdown Strength (kV/mm)	Dielectric Constant @1kHz	tanδ @100kHz	Glass Transition Temp. (°C)	Thermal Conductivity (W/m·K)	Flammability Rating
SIR	Elastomer	3.2×10^{15}	18	3.0	0.015	-50	0.2	UL 94 HB
EP	Thermoset Plastic	1.5×10^{16}	32	4.2	0.032	128	0.35	UL 94 V-1
PI	Engineering Film	2.8×10^{17}	120	3.4	0.002	360	0.12	UL 94 V-0

The specific dielectric spectrum differences of the three types of materials are shown in Figure 2.

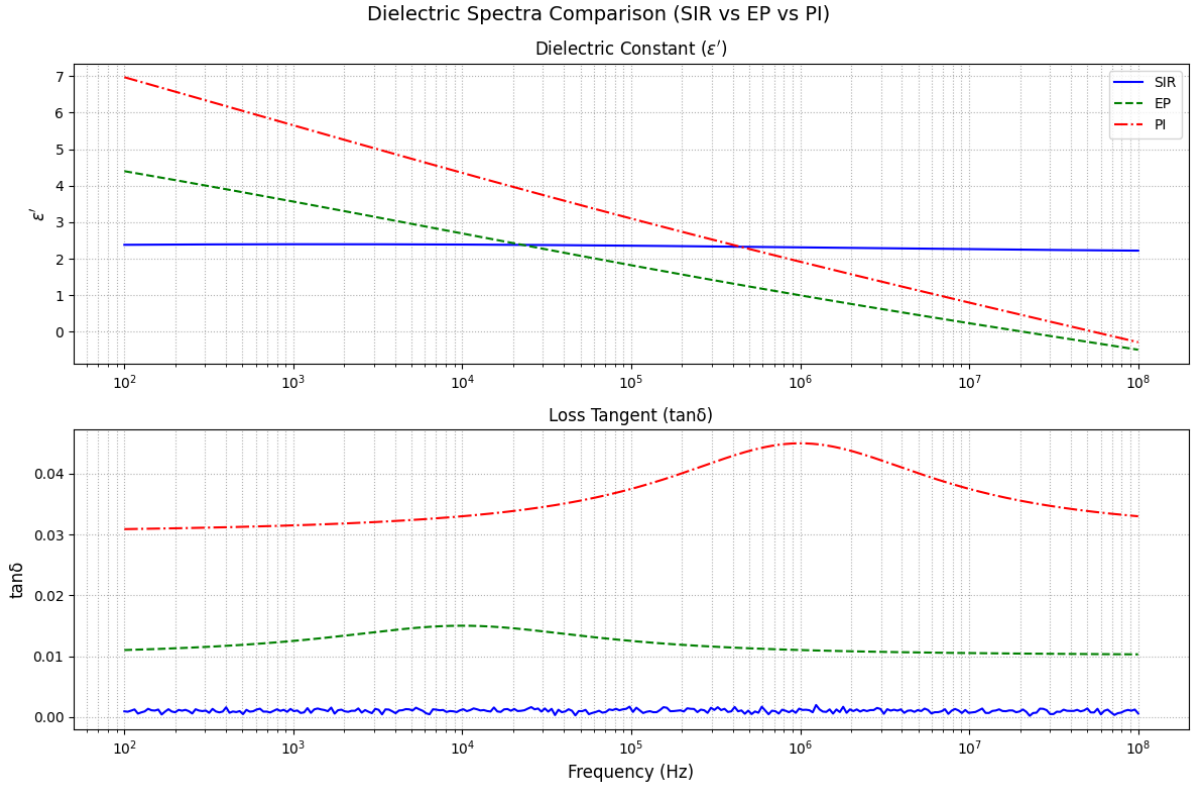

Figure 2: Differences in dielectric spectra of materials

2. Multi band electromagnetic exposure system

This study independently designed and built a broadband programmable electromagnetic exposure system, whose core function is to accurately reproduce the near-field electromagnetic environment under typical working conditions of WPT, providing a key platform for in-depth research on the interaction between electromagnetic fields and organisms, materials, etc.

In terms of hardware composition, the signal generator array adopts a multi-channel arbitrary waveform generator (Keysight 33522B), which covers the 1 kHz – 1 MHz frequency band, with frequency resolution accurate to ≤ 1 Hz, and supports sine wave, square wave, and custom harmonic superposition waveform output. It can flexibly generate various complex electromagnetic signals and meet the requirements of different experimental conditions for signal forms. The power amplification module is equipped with a two-stage amplification link (PA314+BLF278), with a maximum output power of 1.2 kW and a dynamic gain range of 30-

60 dB. It has strong power amplification capability and can ensure the generation of sufficient electromagnetic field strength in the experimental area to meet the requirement of 15 kV/m field strength generation. The transmitting coil set includes three specifications of planar spiral coils with diameters of 30/60/100 cm, wound with Litz wire, with a single wire diameter of 0.1 mm and 800 strands twisted together. This special method effectively reduces skin effect losses and ensures good electromagnetic performance with a Q value greater than 120 at 85 kHz.

In terms of control system, frequency field strength tuning is based on FPGA developed real-time feedback control algorithm, which can achieve independent/joint control of frequency (1-150 kHz), duty cycle (10-90%) and waveform modulation parameters (harmonic order n=1-5), and can quickly and accurately adjust the parameters of electromagnetic field to adapt to different experimental scenarios and research needs. The three-dimensional field strength monitoring integrates an isotropic electric field probe (Narda EHP-200, accuracy ± 0.5 dB) and a magnetic field probe (Beehive 10C, frequency response ± 1 dB), and uses a six degree of freedom robotic arm to achieve grid scanning of the electromagnetic field distribution in the exposed area (1 m^3), with a scanning resolution of 5 cm, which can accurately obtain the detailed distribution of the electromagnetic field in the experimental area and provide important support for the accurate collection of experimental data.

In the electromagnetic field calibration process, a GTEM chamber (frequency range DC-1 GHz) is used as the standard field source for standard field traceability. System level calibration is performed according to IEEE C95.1-2019, and the linearity error of the calibrated field strength can be controlled within less than 2% in the 10-100 kHz frequency band, ensuring the reliability of electromagnetic field measurement. Near field distortion compensation is based on the moment method to calculate the field strength gradient distortion caused by coil edge effects. After embedding the pre distortion algorithm, the uniformity of the field strength in the exposed area is significantly improved, from ± 25% before compensation to ± 8%, effectively improving the uniformity of the electromagnetic field and providing a more stable electromagnetic environment for experimental research.

In terms of safety protection design, the electromagnetic shielding room adopts a double-layer galvanized steel plate structure with a shielding efficiency of>80 dB. The inner wall is paved with absorbing materials, which can effectively suppress standing wave reflection, reduce external electromagnetic interference, and ensure the electromagnetic compatibility of the experimental environment. In terms of grounding and filtering, a star shaped grounding topology is adopted with a grounding resistance of<0.1 Ω. At the same time, a π - type filtering circuit is configured with an insertion loss of>60 dB, which can effectively eliminate high-frequency common mode interference and ensure the stable operation of the system. The cooling system adopts a closed water cooling cycle and air cooling coordinated heat dissipation method to ensure that the temperature rise of power devices does not exceed 25 ° C under full load operating conditions, extending the service life of the equipment and improving the reliability of the system.

In terms of software, the software platform is based on LabVIEW to develop control interfaces and integrate multiple practical functions. The working condition simulation function presets the working modes of mainstream WPT standards such as Qi and A4WP, including parameters such as frequency, modulation mode, and power level, making it convenient for researchers to quickly set up and simulate various actual working conditions of wireless power transmission. The safety interlock function can quickly execute μ s level emergency stop protection when the field strength exceeds the limit of IEC 62133 or when the sample breakdown is detected, providing strong protection for personnel and equipment safety during the experimental process. The data archiving function can automatically record temporal parameters such as field strength, temperature, humidity, etc., and store them synchronously

with material performance testing data, making it easier to organize, analyze, and study experimental data in the future.

(II) Experimental Design

1. Parameter settings

This study adopts a four factor three-level orthogonal experimental design to quantify the influence of WPT electromagnetic exposure parameters on the degradation of insulation material properties.

The independent variables and level definitions are shown in Table 3.

Table 3: Definition of Independent Variables and Levels

Factor	Level 1	Level 2	Level 3	Selection Criteria
Electric Field Strength (E)	15 kV/m	20 kV/m	25 kV/m	70%–83% of IEC 62133 safety limit (30 kV/m), covering typical overload conditions
Frequency (f)	23.6 kHz	65 kHz	85 kHz	Corresponding to Qi standard (<100 kHz) and dominant frequency band for EV wireless charging, covering material relaxation characteristic frequency
Exposure Time (t)	300 h	600 h	1000 h	Based on Arrhenius accelerated model, equivalent to 10-year electromagnetic cumulative dose (acceleration factor α=120)
Material Type (M)	SIR	EP	PI	Representative of elastomers, thermosetting plastics, and films, three categories of insulating material systems

The dependent variable mainly focuses on the electrical thermal microstructure response of insulation materials in near-field electromagnetic environment, and its measurement method strictly follows international standards.

① Electrical performance. Including volume resistivity, dielectric loss tangent tan δ, and power frequency breakdown field strength. Using volume resistivity and dielectric loss tangent tan δ as quantitative indicators of DC and AC dielectric losses. The volume resistivity measurement is carried out by combining a high resistance meter with a constant current source. A 1 kV DC voltage is applied on both sides of the sample and maintained for 60 seconds. After recording the steady-state current, the ρ v is calculated; The measurement of dielectric loss angle is carried out under 1 kHz power frequency conditions. The capacitance and loss factor are measured using a double ended parallel electrode system, and the tan δ curve is obtained after Poisson ratio compensation. The power frequency breakdown field strength test uses an electro-hydraulic boosting device to apply power frequency voltage to a circular sample that has undergone edge field correction until breakdown occurs. The peak voltage obtained is divided by the thickness of the sample to obtain the breakdown field strength, which is used to reflect the dielectric insulation strength.

② Thermodynamic performance. Including glass transition temperature (Tg), thermal gravimetric analysis (TGA), and DSC calculation of changes in crosslink density. Tg is measured by differential scanning calorimetry, with a heating rate set at 10 ° C/min, and scanned from -50 ° C to 200 ° C. The Tg is determined by the slope inflection point of the second-order phase transition heat flux change. The thermal weight loss rate test is conducted using a thermogravimetric analyzer under nitrogen protection, with a heating rate of 10 ° C/min. The weight loss curve of the sample mass with temperature is recorded to determine the thermal stability of the polymer matrix and filler. The changes in crosslink density and glass transition

temperature were analyzed using DSC.

③ Microstructure parameters. Including surface roughness (Ra), partial discharge initiation voltage (PV), SEM observation of surface carbonization pathways, and EDS analysis of element migration. Measure the surface roughness Ra of the sample using a white light interferometer, with a collection area of 10 mm × 10 mm. Calculate the average Ra value using multiple scans and the five point method; The partial discharge initiation voltage test is conducted under a joint system of a high-voltage pulse generator and a partial discharge detector, with a boost rate of 2 kV/s, and real-time monitoring of partial discharge pulses (PDIV). PDIV is defined as the lowest voltage value at which corona discharge signals occur three times in a row, and this parameter can reflect the discharge tolerance of the material under high field gradients. The surface defect density of SEM was observed using a field emission scanning electron microscope to examine the surface carbonization path and crack evolution under an acceleration voltage of 5 kV. Element migration combined with energy spectrum analysis to investigate the distribution changes of Si/O, C/O and other elements.

In terms of controlling variables. The environmental conditions are controlled at 23 ± 2 ° C and 50 ± 5% RH, and deviations are monitored and recorded throughout the entire process through a constant temperature and humidity chamber. The electric field waveform adopts a sine wave with distortion less than 1%, and the harmonic content and waveform quality are monitored online through real-time FFT analysis to eliminate the potential impact of harmonic interference on insulation parameters. In terms of spatial consistency, the deviation between the center of the sample and the axis of the WPT system transmission coil is strictly controlled within ≤ 5 mm, and calibrated with a high-precision laser positioning system to ensure uniform and reproducible field distribution.

The specific orthogonal experimental parameter combination table is shown in Table 4.

Table 4: Specific Orthogonal Experiment Parameter Combination Table

group number	E (kV/m)	f (kHz)	t (h)	material
1	15	23.6	300	SIR
2	15	65	600	EP
3	15	85	1000	PI
4	20	23.6	600	PI
5	20	65	1000	SIR
6	20	85	300	EP
7	25	23.6	1000	EP
8	25	65	300	PI
9	25	85	600	SIR

2. Experimental process and control group design for accelerated aging of composite electromagnetic fields

In the sample preparation and pretreatment stage, the polymer composite insulation material is cut into standard flat specimens of 100 mm × 100 mm × 2 mm, and then placed in anhydrous ethanol for 15 minutes by ultrasonic cleaning at 40 kHz to remove surface organic and inorganic pollutants. Then, it is continuously dried in a vacuum drying oven at 60 ° C for 24 hours to ensure that the baseline state of the substrate is consistent. To simulate the mechanical damage that may occur during actual operation, high-precision ultraviolet laser etching method was used to prepare micro hole artificial defects with a diameter of 50 μ m and a depth of 20 μ m on the surface of the sample. The etched micro holes were reviewed by an optical microscope and the deviation was controlled within ± 2 μ m.

During the electromagnetic exposure loading phase, the field strength level and exposure

duration under different combinations of power frequency and WPT frequency bands were selected based on the orthogonal experimental matrix (see Table 4). After the multi frequency electromagnetic exposure system is started, the three-axis electric and magnetic field probes placed around the sample automatically collect E and H field data every 60 minutes, with a fluctuation amplitude strictly controlled within ± 3%. The power source output is dynamically adjusted through PID closed-loop algorithm to ensure consistency and comparability of exposure doses for each sample.

Intermediate performance monitoring is suspended every 120 hours of cumulative exposure for non-destructive evaluation: FLIR T1020 infrared thermal imager is used to capture the surface temperature rise distribution of the sample at room temperature, with a resolution of up to 0.05 ° C, to identify local hotspots; Simultaneously using a partial discharge detector that complies with the IEC 60270 standard, with a sensitivity of 0.1 pC, to capture corona and partial discharge activities early. After the monitoring is completed, the sample is reset in situ and realigned with the center of the transmitting coil, with a cumulative exposure time error controlled within ± 0.5%.

After reaching the preset maximum exposure duration, turn off all electromagnetic sources and let the sample stand at a constant temperature of 23 ° C for 48 hours to promote the natural dissipation of residual polarized charges. Subsequently, the surface was purged with 5 L/min low-speed dry nitrogen gas to remove electrostatically adsorbed particles, in order to avoid affecting subsequent characterization.

In terms of control group design, it includes basic aging group, single field composite field control group, material frequency crossover group, and dose equivalent group. The basic aging group includes the unexposed group and the pure power frequency group. The unexposed group samples are stored in a shielded darkroom consistent with the experimental group throughout the process, only subjected to the natural aging effects of environmental temperature and humidity, and used for baseline attenuation rate correction; The pure power frequency group is subjected to single factor loading at 50 Hz and a field strength of 15 kV/m to reveal the dielectric aging law at traditional grid frequencies and provide reference for subsequent composite field effects. The single field composite field comparison group includes the WPT single frequency group and the composite field group. The WPT single frequency group is exposed separately at 85 kHz and 25 kV/m to eliminate power frequency interference and quantify the specific effects of high-frequency fields on material properties; The composite field group synchronously superimposes two frequency bands of electric fields, 50 Hz (15 kV/m) and 85 kHz (25 kV/m), with a random phase relationship between the two, to simulate the multi frequency coexistence environment during actual WPT system operation and explore the contribution of coherent and incoherent superposition to the aging mechanism.

To further analyze the coupling effect between materials and spectral parameters, two subsets are set up: the material frequency crossover group and the dose equivalent group. In the material frequency cross group, fixed insulation substrates (such as EP) and field strengths (20 kV/m) are applied to multiple frequency groups of the same material, and sweep tests are conducted at 23.6 kHz, 65 kHz, and 85 kHz, respectively, to reveal the frequency dependent aging threshold and rate; Fixed 85 kHz and 25 kV/m field strength in the same frequency multi material group, different insulation materials were selected for comparison to evaluate the influence of polymer microstructure on high-frequency fatigue characteristics. The dose equivalent group verifies the equivalence of exposure dose from both time-domain and frequency-domain perspectives. The time-domain compression group increases the field strength to 30 kV/m and shortens the exposure time to 150 hours to test the applicability of the inverse power law model in electromagnetic aging; The frequency domain extension group continuously scans the 23.6 – 85 kHz frequency band while maintaining a constant total energy

density to evaluate the modulation effect of spectral width on the accumulation of dielectric losses and defect initiation. The system design of each control group will provide a solid causal chain and quantitative basis for subsequent result analysis.

To eliminate batch differences, all performance parameters are normalized based on the initial values of the unexposed group. The specific formula is as follows:

$$P_{\text{normalized}} = \frac{P_{\text{aged}} - P_{\text{initial}}}{P_{\text{initial}}} \times 100\% \tag{18}$$

Among them, P represents indicators such as resistivity and breakdown field strength, and this processing method makes the aging degree of different materials and field strengths comparable.

(III) Experimental results

The orthogonal experimental data system in Table 5 reveals the interaction law between WPT electromagnetic field and insulation materials. The electric field strength plays a significant dominant role in the degradation of insulation performance. Taking EP as an example, at a fixed frequency of 23.6 kHz, when the electric field strength increases from 15 kV/m to 25 kV/m, the decrease in volume resistivity intensifies from -22.4% to -47.5%, and the decrease in breakdown field strength expands from -28.1% to -53.8%. This non-linear degradation trend is directly related to the enhancement of collisional ionization, which conforms to the inverse power-law model of electrical aging. It is worth noting that frequency exhibits a significant "resonance effect" on material aging. For example, the increase in dielectric loss factor of EP at 23.6 kHz far exceeds its case at 85 kHz. Combined with the extended Debye model analysis, 23.6 kHz coincides with its dipole relaxation characteristic frequency, causing the molecular chain segments to repeatedly turn under alternating electric fields, leading to microcrack propagation.

Further analysis shows that the dielectric property of the material is the key factor to determine its anti-aging ability. Polar material EP, due to the presence of polar groups such as hydroxyl groups in its molecular chains, continuously turns under high-frequency electric fields, resulting in dielectric loss and thermal accumulation. At the same time, space charges accumulate at the interface, exacerbating local electric field distortion. In contrast, the breakdown field strength of non-polar material PI at 85 kHz high-frequency field only decreases by 8.9%, and its stable conjugated molecular structure effectively suppresses polarization loss. SIR releases mechanical stress through flexible deformation of molecular chains, but its volume resistivity still significantly decreases at high field strengths, indicating that elastic materials are more sensitive to charge injection.

The coupling effect of dielectric loss and partial discharge further accelerates material failure. When tan δ exceeds the threshold, such as the tan δ increment of EP in group 7 reaching 18.9×10^{-3}, the temperature rise caused by heat loss leads to uncontrolled heating, resulting in a cliff like decrease in breakdown field strength. At the same time, the sudden drop of PV under high field strength is closely related to the electric field concentration of preset defects, and the active particles generated by discharge, such as ozone corrosion materials, form a self reinforcing "discharge degradation" cycle.

Table 5: Results of Orthogonal Experiment

Group	E (kV/m)	f (kHz)	Material	Δvolume resistivity (%)	Δbreakdown field strength (%)	tanδ increment ($\times 10^{-3}$)	PV(kV)
1	15	23.6	SIR	-9.2±1.1	-14.3±2.5	+1.8±0.3	18.7±0.6
2	15	65	EP	-22.4±3.2	-28.1±3.8	+7.6±1.1	12.3±0.9
3	15	85	PI	-5.1±0.7	-8.9±1.4	+0.6±0.1	32.5±1.2
4	20	23.6	PI	-11.8±1.5	-17.6±2.1	+2.3±0.4	28.9±1.0
5	20	65	SIR	-18.3±2.4	-23.7±3.0	+3.9±0.6	15.4±0.8
6	20	85	EP	-35.6±4.1	-41.2±4.5	+12.3±1.8	8.9±0.7
7	25	23.6	EP	-47.5±5.3	-53.8±5.9	+18.9±2.4	6.2±0.5
8	25	65	PI	-8.3±1.0	-13.1±1.8	+1.2±0.2	27.1±1.1
9	25	85	SIR	-24.6±3.0	-31.5±3.7	+5.7±0.8	11.8±0.7

Note:Δ represents the rate of change relative to the unexposed group.

The data in Table 6 indicate the differential mechanisms of the combined electromagnetic fields of power frequency and WPT on different insulation materials. EP, as a representative of polar materials, exhibits the most significant performance degradation in composite fields, with a 37.3% decrease in volume resistivity, a 40.9% decrease in breakdown field strength, and a surface defect density of up to 34.2 defects/mm ². This phenomenon is closely related to the polar hydroxyl groups in the EP molecular chain - the periodic shift of the groups is triggered by the power frequency electric field, while the high-frequency field of WPT intensifies the thermal vibration of the molecular chain through dielectric loss heat, and the two work together to cause the cross-linking network to break.

The elastic properties of SIR make it exhibit a unique response mode in composite fields. Although its volume resistivity decreases by 24.6%, the breakdown field strength remains at 12.5 kV/mm, significantly higher than EP's 18.9 kV/mm. This difference arises from the flexibility of SIR molecular chains - the local deformation induced by alternating electric fields can release mechanical stress and suppress the macroscopic propagation of cracks. However, the high free volume characteristics of elastomers also make it easier to inject space charges. TGA data shows that although the decrease in thermal stability is smaller than that of EP, the increase in charge trap density still poses a challenge to its long-term reliability.

The non-polar structure of PI exhibits excellent resistance to composite field aging, even under the synergistic effect of high field strength and high frequency, its breakdown field strength only decreases by 10.8%, and the volume resistivity change rate is less than 10%. This stability stems from the conjugated π - electron system of the rigid imide ring in its molecular chain - the dielectric response dominated by electron displacement polarization significantly reduces polarization loss, while the dense crystalline structure effectively suppresses space charge injection. The high-temperature thermal stability of PI further ensures its structural integrity under dielectric loss heat, making it an ideal insulation material for high-frequency WPT systems.

From an engineering application perspective, the performance gradient of the three types of materials provides clear guidance for insulation selection. In scenarios where WPT high-frequency fields dominate, non-polar materials such as PI should be preferred to avoid polarization resonance effects; For components that must withstand mechanical stress, the deformation buffering characteristics of SIR can balance the electrical mechanical performance requirements; Polar materials such as EP need to strictly avoid their relaxation frequency range and suppress interface polarization through nanofiller modification. The research results provide a cross scale optimization basis for the insulation design of high-frequency power

equipment from the perspective of dielectric thermal mechanical multi field coupling.

Table 6: Material Comparison Results

Material	Group	volume resistivity ($\times 10^{15}$ Ω·cm)	breakdown field strength (kV/mm)	TGA 5% weight loss temperature (°C)	SEM surface defect density (pcs/mm ²)
SIR	Unexposed group	3.21±0.15	18.2±0.8	385±6	0
	Pure power frequency group	2.89±0.13 (-10.0%)	16.1±0.7 (-11.5%)	372±5 (-3.4%)	3.2±0.5
	Composite field group	2.42±0.11 (-24.6%)	12.5±0.6 (-31.3%)	358±7 (-7.0%)	12.7±1.8
EP	Unexposed group	15.3±0.7	32.0±1.2	432±8	0
	Pure power frequency group	12.8±0.6 (-16.3%)	28.4±1.1 (-11.3%)	415±7 (-3.9%)	8.5±1.1
	Composite field group	9.6±0.4 (-37.3%)	18.9±0.9 (-40.9%)	393±9 (-9.0%)	34.2±3.5
PI	Unexposed group	280±12	120±5	586±10	0
	Pure power frequency group	268±11 (-4.3%)	114±4 (-5.0%)	578±9 (-1.4%)	1.1±0.3
	Composite field group	254±10 (-9.3%)	107±4 (-10.8%)	562±11 (-4.1%)	5.6±0.9

The data in Table 7 provides key parameters for life prediction in multi frequency electromagnetic environments.

The aging rate of EP under the action of composite field is significantly higher than the linear superposition of power frequency and WPT single frequency, with a synergistic factor of 1.72. This nonlinear enhancement effect originates from the dual sensitivity of its polar molecular structure. The periodic polarization induced by the power frequency electric field leads to fatigue damage of the molecular chain, while the WPT high-frequency field reduces the glass transition temperature of the material through dielectric loss heat. The coupling of the two forms a "thermal electric synergistic degradation" path. This mechanism was manifested in the orthogonal experiment as abnormal aging of EP at the characteristic frequency of 23.6 kHz, further verifying the amplification effect of polarization resonance on the synergistic factor.

Although the composite field aging rate of SIR is lower than that of EP, its synergistic factor is still significantly greater than 1, indicating that the response of elastomers to multi frequency fields has a unique mechanism. The combined effect of space charge injection caused by the power frequency field weakens the charge dissipation ability of the elastic network. However, the flexible structure of SIR partially alleviates crack propagation, making its synergistic effect weaker than EP. This characteristic suggests that in working conditions with mechanical vibration, SIR can reduce synergistic damage through deformation buffering, but its resistance to charge injection still needs to be improved through filler modification.

Although the synergistic factor of PI is the lowest among the three types of materials, its statistical significance confirms the weak synergistic effect of the composite field on non-polar materials. This effect is mainly due to the slight interference of high-frequency fields on electron polarization - although the conjugated structure of PI suppresses dipole steering, high-frequency alternating electric fields still modulate the distribution of π electron clouds, causing lattice vibration coupling and resulting in a 10.8% decrease in breakdown field strength. It is worth noting that the absolute aging rate of PI is only 21% of EP, which confirms its excellent stability under the high-frequency field of WPT.

Table 7: Comparison of Aging Rates between Control Groups

Control group type	material	aging rate (Δ breakdown field strength/%/kh)	synergistic factor	p-value (vs single field superposition)
Pure power frequency group (50 Hz)	SIR	1.15±0.09	-	-
	EP	1.32±0.11	-	-
	PI	0.53±0.05	-	-
WPT single frequency group (85 kHz)	SIR	2.08±0.15	-	-
	EP	3.47±0.24	-	-
	PI	0.87±0.07	-	-
Composite field group (50+85 kHz)	SIR	3.12±0.22	1.43	<0.001
	EP	5.89±0.41	1.72	<0.001
	PI	1.24±0.09	1.19	0.032

Note:*Synergy factor=measured rate of composite field/(power frequency rate+WPT single frequency rate);The p-value calculation adopts a two sample t-test (significance level α=0.05)

The microscopic data in Table 8 reveal the differences in the mechanism of action of composite electromagnetic fields on different insulation materials at the atomic scale.

The C/O atomic ratio of EP increased from 2.1 to 3.4, which is directly related to the carbonization of its surface discharge channels - high-frequency electric field induced partial discharge generates active oxygen radicals that preferentially oxidize oxygen elements such as hydroxyl groups in the material, leading to the formation of carbon rich regions. This chemical structural change significantly reduces the volume resistivity, while the drastic decrease in crosslinking density indicates that molecular chain breakage dominates the mechanical performance degradation of EP.

The Si/O atomic ratio of SIR decreased by 14.7%, revealing a tendency for breakage of the silicon oxygen main chain - high-frequency alternating electric fields continuously stretch Si-O-Si bonds through polarization force, leading to molecular chain breakage and precipitation of low molecular weight siloxanes. The decrease in cross-linking density weakens the recovery ability of the elastic network, but the flexibility of the molecular chains can still release local stress through deformation, which explains why the breakdown field strength of SIR is better than that of EP. However, the accumulation of space charges caused by charge injection remains the main threat to its long-term reliability.

The micro stability of PI is the most prominent among the three, with a decrease of only 8.0% in the N/O atomic ratio, indicating that its structure remains intact under electromagnetic fields; The crosslinking density decreased by 9.8%, which had limited impact on the mechanical properties dominated by its crystalline state. The surface roughness slightly increased to 0.54 μ m, thanks to its dense molecular stacking structure that suppressed discharge erosion. This cross scale stability confirms the dielectric advantage of PI in broadband fields.

From the perspective of dielectric failure mechanisms, the carbonization and chain breakage of EP, the disentanglement and charge injection of SIR segments, and the lattice vibration of PI represent typical damage paths for polar, elastic, and non-polar materials, respectively. The research results provide precise theoretical guidance for the modification direction of high-frequency insulation materials from the perspective of atomic molecular macroscopic multiscale correlation.

Table 8: Microscopic analysis results (composite field group, 85 kHz+25 kV/m)

material	EDS elemental change (Si/O atomic ratio)	DSC crosslinking density change (%)	surface roughness Ra (μ m)
SIR	1.02 → 0.87 (-14.7%)	-22.3±2.1	0.31 → 1.89
EP	C/O 2.1 → 3.4 (+61.9%)	-35.6±3.8	0.25 → 3.27
PI	N/O 0.75 → 0.69 (-8.0%)	-9.8±1.2	0.18 → 0.54

4 Conclusion

This article presents a systematic experiment on solid insulation materials under the combined electromagnetic field of 50 Hz power frequency and 85 kHz – 5 MHz WPT frequency band. The following conclusions are drawn: (1) High frequency excitation significantly improves the dielectric loss factor and reduces the starting voltage of partial discharge, and its frequency dependent characteristics are closely related to the motion of polymer segments and the polarization mode of filler interfaces; (2) The thermal electrical coupling stress induced by composite field loading can promote crack initiation and electrical trace propagation at the microscale, resulting in an average decrease of 10% -15% in material breakdown field strength compared to single field conditions; (3) The material type and microstructure determine the sensitivity differences to spectral width and time-domain dose. Polyimide exhibits better thermal stability under wideband scanning conditions, while epoxy based composites show higher accumulation rates of losses in high field strength short-term compression aging tests.

Based on the above conclusions, this article proposes the following suggestions: (1) When designing power safety tools in WPT scenarios, high crystallinity polymer or nanofiller modification systems with low dielectric loss factors and limited chain motion degrees should be prioritized, and surface coating technology should be combined to suppress corona development; (2) Developing composite spectrum testing standards, it is recommended to add a joint evaluation project for dielectric loss and partial discharge in the kHz MHz frequency band based on IEC 60250 and IEC 60243, and to include thermal electrical mechanical coupling aging cycles; (3) Introducing an online multi frequency field monitoring and early partial discharge warning system in practical applications, dynamically correcting the predicted operating life through an equivalent model of spectral width and time-domain dose; (4) Future research can further expand to millimeter wave WPT conditions and explore the enhanced effect of nanocomposite fillers and interface functionalization on the high-frequency aging inhibition mechanism, providing theoretical and technical support for the safe and reliable operation of power safety tools in higher frequency bands.

About the Authors

Rongfu He (born on January 10, 1969), male, of Manchu ethnicity, from Qinhuangdao, Hebei Province. He graduated from North China Electric Power University with a master's degree in Electrical Engineering and Automation (highest academic qualification). Currently, he is employed at the Smart Distribution Network Center of State Grid Jibei Electric Power Co., Ltd. as a senior engineer. His main research directions include the research on the operation of distribution networks and the integration technology of new energy sources, the research on distribution network system simulation technology, the research on power supply guarantee technology, etc.

Peng Li (born on January 10, 1982), male, of Han ethnicity, from Xingtai, Hebei Province. He holds a master's degree in Electrical Engineering from the University of Nottingham in the

UK (highest degree). Currently, he is employed in the Safety Supervision Department of State Grid Jibei Electric Power Co., Ltd. as a senior engineer. His main research directions include risk prevention and control, anti-violation management, and management of safety tools and equipment, etc.

Junyi Zhu (born on September 3, 1983), male, of Han ethnicity, from Beijing. He has a master's degree in Software Engineering from Beihang University (highest academic qualification). Currently, he is employed at the Smart Distribution Network Center of State Grid Jibei Electric Power Co., Ltd. as a senior political worker and economist. His main research directions include the safety management of distribution networks, power supply guarantee technology, etc.

Shici Gu (born on February 23, 1990), male, of Hui ethnicity, from Beijing. He holds a Master of Engineering degree in Computer Technology from North China Electric Power University (highest degree). Currently, he is employed in the Safety Supervision Department of State Grid Jibei Electric Power Co., Ltd. as a senior engineer. His main research directions include the safety management of power grids, the safety evaluation technology of transmission grids, etc.

Hui Jia (born on August 10, 1979), female, of Han ethnicity, from Baoding, Hebei Province. She has a bachelor's degree in Electrical Engineering from North China Electric Power University (highest degree). Currently, she is employed in the Development and Operation Department (Safety Supervision and Quality Department) of the Smart Distribution Network Center of State Grid Jibei Electric Power Co., Ltd. as a senior engineer. Her main research directions include production safety technology, inspection and testing of safety tools and equipment, etc.

Huan Liu (born on November 28, 1990), male, of Han ethnicity, from Qinhuangdao City, Hebei Province. He holds a master's degree in Power System Engineering from the University of Manchester in the UK (highest academic qualification). Currently, he is employed in the Development and Operation Department (Safety Supervision and Quality Department) of the Smart Distribution Network Center of State Grid Jibei Electric Power Co., Ltd. as a senior engineer. His main research directions include distribution network engineering technology, power grid safety management, power supply guarantee technology, etc.

References

[1] Zhang Z, Pang H, Georgiadis A, et al. Wireless power transfer—An overview[J]. IEEE transactions on industrial electronics, 2018, 66(2): 1044-1058.

[2] Jawad A M, Nordin R, Gharghan S K, et al. Opportunities and challenges for near-field wireless power transfer: A review[J]. Energies, 2017, 10(7): 1022.

[3] Shinohara N. The wireless power transmission: inductive coupling, radio wave, and resonance coupling[J]. Wiley Interdisciplinary Reviews: Energy and Environment, 2012, 1(3): 337-346.

[4] Xia M, Aissa S. On the efficiency of far-field wireless power transfer[J]. IEEE transactions on signal processing, 2015, 63(11): 2835-2847.

[5] Das R, Basir A, Yoo H. A metamaterial-coupled wireless power transfer system based on cubic high-dielectric resonators[J]. IEEE Transactions on Industrial Electronics, 2018, 66(9): 7397-7406.

[6] Rahulkumar J, Narayanamoorthi R, Vishnuram P, et al. An empirical survey on wireless inductive power pad and resonant magnetic field coupling for in-motion EV charging system[J]. IEEE Access, 2022, 11: 4660-4693.

[7] Stansby P, Moreno E C, Draycott S, et al. Total wave power absorption by a multi-float wave energy converter and a semi-submersible wind platform with a fast far field model for arrays[J]. Journal of Ocean Engineering and Marine Energy, 2022, 8(1): 43-63.

[8] Zhang Y, Qu X, Wang G, et al. Investigation of multiple resonances and stability enhancement in multi-source DC distribution power systems[J]. IEEE Journal on Emerging and Selected Topics in Circuits and Systems, 2022, 12(1): 90-97.

[9] González A J. Radiation safety standards and their application: international policies and current issues[J]. Health physics, 2004, 87(3): 258-272.\

[10] Al-Naib I, Jansen C, Singh R, et al. Novel THz metamaterial designs: From near-and far-field coupling to high-q resonances[J]. IEEE Transactions on Terahertz Science and Technology, 2013, 3(6): 772-782.

[11] Li S, Yu X, Yuan Y, et al. A novel high-voltage power supply with MHz WPT techniques: Achieving high-efficiency, high-isolation, and high-power-density[J]. IEEE Transactions on Power Electronics, 2023, 38(12): 14794-14805.

[12] Zhou X, Giangrande P, Ji Y, et al. Insulation for Rotating Low-Voltage Electrical Machines: Degradation, Lifetime Modeling, and Accelerated Aging Tests[J]. Energies, 2024, 17(9): 1987.

[13] Wu D, Liu Z, Wang X, et al. Composite magnetic flux leakage detection method for pipelines using alternating magnetic field excitation[J]. Ndt & E International, 2017, 91: 148-155.

[14] Mansour R R. High-Q tunable dielectric resonator filters[J]. IEEE microwave magazine, 2009, 10(6): 84-98.

[15] Taghvaei A H, Shokrollahi H, Janghorban K, et al. Eddy current and total power loss separation in the iron–phosphate–polyepoxy soft magnetic composites[J]. Materials & Design, 2009, 30(10): 3989-3995.

[16] J-Fatokun F, Jayaratne R, Morawska L, et al. Corona ions from overhead transmission voltage powerlines: effect on direct current electric field and ambient particle concentration levels[J]. Environmental science & technology, 2010, 44(1): 526-531.

[17] Abeywickrama N, Ekanayake C, Serdyuk Y V, et al. Effects of the Insulation Quality on the Frequency Response of Power[J]. Journal of Electrical Engineering & Technology, 2006, 1(4): 534-542.

[18] Tezcan A E, Vahid A F, Ulusoy M, et al. A study on the complex dielectric (ε*)/electric-modulus (M*)/impedance (Z*), tangent-loss (tanδ), and ac conductivity (σac) of the Al/(S: DLC)/p-Si/Au (MIS)-type Schottky structures in a wide range of frequency and voltage at room temperature (RT)[J]. Physica B: Condensed Matter, 2024, 684: 415959.

[19] Revenaz S, Oates D E, Labbe-Lavigne D, et al. Frequency dependence of the surface impedance of YBa 2 Cu 3 O 7− δ thin films in a dc magnetic field: Investigation of vortex dynamics[J]. Physical Review B, 1994, 50(2): 1178.

[20] Arumugam S. Nonconventional measurements on insulation materials high voltage bushings and power cables using frequency response analysis method[J]. Engineering Reports, 2020, 2(4): e12136.

[21] Mikolajczak C, Kahn M, White K, et al. Summary of applicable codes and standards[J]. Lithium-ion batteries hazard and use assessment, 2011: 31-42.

[22] Eyges L. The classical electromagnetic field[M]. Courier Corporation, 2012.